Eruptive Event Generator Based on the Gibson-Low Magnetic Configuration

D. Borovikov, [1] I. V. Sokolov, [1] W. B. Manchester, [1] M. Jin, [2,3] and T. I. Gombosi, [1]

[1] Center for Space Environment Modeling, University of Michigan, 2455 Hayward St, Ann Arbor, MI 48109, USA; dborovik@umich.edu, igorsok@umich.edu, chipm@umich.edu, tamas@umich.edu.

[2] Lockheed Martin Solar and Astrophysics Lab, Palo Alto, CA 94304, USA; jinmeng@lmsal.com

[3] Cooperative Programs for the Advancement of Earth System Science (CPAESS), University Corporation for Atmospheric Research (UCAR), Boulder, CO 80307

Abstract

Coronal Mass Ejections (CMEs), a kind of energetic solar eruptions, are an integral subject of space weather research. Numerical magnetohydrodynamic (MHD) modeling, which requires powerful computational resources, is one of the primary means of studying the phenomenon. With increasing accessibility of such resources, grows the demand for user-friendly tools that would facilitate the process of simulating CMEs for scientific and operational purposes. The Eruptive Event Generator based on Gibson-Low flux rope (EEGGL), a new publicly available computational model presented in this paper, is an effort to meet this demand. EEGGL allows one to compute the parameters of a model flux rope driving a CME via an intuitive graphical user interface (GUI). We provide a brief overview of the physical principles behind EEGGL and its functionality. Ways towards future improvements of the tool are outlined.

Coronal Mass Ejections (CMEs) were first observed in the early 1970s. The phenomenon immediately drew attention of the scientific community and stayed in focus because of the potential hazards that CMEs pose to humanity, its technology and endeavors [*Webb*, 1995, 2000; *Gopalswamy*, 2009]. Bodies of works studying either subject constitute two whole branches of physical research [see e.g. *Cliver*, 2009; *Lakhina and Tsurutani*, 2016]. The vast range of damage that CMEs may cause highlights how crucial is the ability to mitigate their effects, which may be attained with the forecasting capability in studies of CMEs and their propagation to Earth..

Efforts aimed at developing predictive models include various empirical and statistical models some of which are designed to predict the arrival time of a CME at 1 AU, such as ElEvoHI [*Rollett et al.*, 2016] and a number of others [e.g. *Gopalswamy et al.*, 2001; *Riley et al.*, 2015]. The most significant problem in space weather forecasting at the moment, however, is determining the magnetic field and its southward component, B_z, in particular in an Earth-impacting CME. Among promising recent models that predict B_z are, for example, *Savani et al.* [2015]; *Kay et al.* [2017]. Despite great advancements in empirical techniques, such models are naturally limited in both accuracy and amount of information they are able to provide. Significant complex processes such as CME deflection and rotation caused by interaction with the coronal magnetic field, are inevitably significantly simplified or even omitted in these models. For this reason fully 3-D numerical modeling remains the most promising tool utilized in CME forecasting. These simulations are able to provide predictions for CME arrival time, structure and, most importantly, the magnetic field vector, while taking fully into account complexity of the aforementioned processes.

Over last two decades a very prominent progress has been made in this area. Several so-called kinematic CME models have been developed, e.g. Hakamada-Akasofu-Fry version 2 (HAFv.2) model [*Hakamada and Akasofu*, 1982; *Fry et al.*, 2001; *Dryer et al.*, 2004] and the cone model [*Zhao et al.*, 2002; *Hayashi et al.*, 2006], which accurately predict the CME arrival time (typically within 8 to 10 hours), although they aren't able to predict CME's plasma parameters. Further, the geometric and kinematic properties of a CME found with the cone model are often used as an input for ENLIL [*Odstrčil*, 2003], a 3-D MHD heliospheric model. Such combination allows obtaining more detailed results for CME-caused disturbances of plasma parameters, e.g. density and pressure, but lacks accuracy in predicting the magnetic field.

As CME models grew in complexity, due to major advancements in numerical methods and computing capabilities, a new type of challenge has emerged. It became increasingly difficult for an individual researcher to be able to apply these sophisticated computational tools in their work. For this reason, there has been an effort to simplify the access to the models and thus make the modeling of CMEs a more available and frequent practice. An important step towards these goals is the Eruptive Event Generator based on Gibson-Low magnetic configuration (EEGGL).

EEGGL is a supporting numerical tool that provides parameters for an independent CME model, which employs the *Gibson and Low* [1998] (GL) flux rope configuration. This approach inserts the GL flux rope into a numerical model of the corona. It has been applied in a number of works [*Manchester et al.*, 2004a,b, 2006, 2014b,a; *Lugaz et al.*, 2005, 2007; *Kataoka et al.*, 2009; *Jin et al.*, 2016, 2017a; *Shiota and Kataoka*, 2016] and has proved to be well-suited for the purposes of simulating CMEs. The GL flux rope serves as a good representation of an erupting magnetic flux rope filled with dense plasma that is representative of a filament. This flux rope expands and evolves into a magnetic cloud as it propagates away from the Sun, which provides the basis for simulating magnetically driven CMEs to 1 AU. We emphasize that by choosing GL configuration we don't claim its superiority over alternatives [e.g. *Titov and Démoulin*, 1999].

The key idea of constructing a GL flux rope is to convert a spherical magnetic configuration in equilibrium, the spheromak, into a self-similarly expanding flux rope in the presence of gravity. In the MHD equilibrium, the magnetic field $\mathbf{B}$, current density, $\mathbf{j}$, and plasma pressure, P, satisfy equation [*Landau and Lifshitz*, 1960]:

$$\mathbf{j} \times \mathbf{B} - \nabla P = 0, \tag{1}$$

For any equilibrium configuration, $\mathbf{j} \cdot \nabla P = 0$ and $\mathbf{B} \cdot \nabla P = 0$, i.e. a single line of either magnetic field, or electric current is entirely confined within a single *magnetic surface*, which is a surface of constant pressure. For an axisymmetric equilibrium MHD configuration the relation between the magnetic field, current and pressure is further strengthened. The magnetic flux, ψ, and the current, I, bounded by the magnetic surface remain constant at this surface, just as the pressure. Therefore, there is a functional dependence between ψ, I and P: I=$I(\psi)$, P=$P(\psi)$. Under these circumstances, the magnetic field is governed by the Grad-Shafranov equation [*Grad and Rubin*, 1958; *Shafranov*, 1966]. In the particular case of constant $\frac{dI}{d\psi}$ and $\frac{dP}{d\psi}$, the Grad-Shafranov equation has analytical solutions. One such solution describes the spheromak configuration, bounded by a spherical magnetic surface, $\|\mathbf{R}-\mathbf{R}_\mathrm{s}\| = r_0$. Its magnetic field and pressure may be parameterized via three constant parameters B_0, $\alpha_0 = \mu_0 dI/d\psi$ and $\beta_0 = \frac{\mu_0}{B_0\alpha_0^2}\frac{dP}{d\psi}$ as follows:

$$\mathbf{B}_\mathrm{s}(\mathbf{r}) = \left[\frac{j_1(\alpha_0 r)}{\alpha_0 r} - \beta_0\right](2\mathbf{B}_0 + \sigma_h\alpha_0[\mathbf{B}_0\times\mathbf{r}]) + j_2(\alpha_0 r)\frac{[\mathbf{r}\times[\mathbf{r}\times\mathbf{B}_0]]}{r^2} \tag{2}$$

$$P_\mathrm{s}(\mathbf{r}) = \left[\frac{j_1(\alpha_0 r)}{\alpha_0 r} - \beta_0\right]\frac{\beta_0\alpha_0^2[\mathbf{r}\times\mathbf{B}_0]^2}{\mu_0} \tag{3}$$

$j_1(x) = \frac{\sin x - x\cos x}{x^2}$ and $j_2(x) = \frac{3j_1(x)-\sin x}{x}$ are the spherical Bessel functions of argument x=$\alpha_0 r$, $\sigma_h = \pm1$ is the sign of helicity. Herewith, the vector $\mathbf{B}_0$ is introduced with the magnitude equal to B_0 directed along the axis of symmetry. In Eqs. 2-3, the coordinate vector, $\mathbf{r}$, originates at the center of configuration, $\mathbf{R}_\mathrm{s}$ [1]. Generally, the coordinate vector, $\mathbf{R}$, is related to $\mathbf{r}$ as $\mathbf{r} = \mathbf{R} - \mathbf{R}_\mathrm{s}$.

At the external boundary, $\|\mathbf{R}-\mathbf{R}_\mathrm{s}\| = r_0$, the radial and toroidal components of the magnetic field vanish (i.e. $j_1(\alpha_0 r_0) = \beta_0\alpha_0 r_0$). Thus, for a given β_0 the configuration size, r_0, is related with the extent of magnetic field twisting, α_0, needed to close the configuration within this size. The plasma pressure, P, also turns to zero at the external boundary. In *Gibson and Low* [1998] and the papers cited therein, the non-trivial choice of *negative* value of β_0 had been proposed (without stating this point explicitly), such that all three components in Eq. 2 vanish at $\|\mathbf{R}-\mathbf{R}_\mathrm{s}\| = r_0$. Specifically, the choice of β_0=$j_1(\alpha_0 r_0)/(\alpha_0 r_0)\approx -2.87\cdot 10^{-2}$, where the radius is defined by condition $j_2(\alpha_0 r_0)$=0, i.e. $\alpha_0 r_0\approx 5.76$, satisfies this criterion.

The negative variation of pressure within the configuration as in Eq. 3 is meaningful only when added to some positive background pressure, P_b, so that the total pressure, P_s+P_b, is positive and realistic. To avoid the pressure jump at the boundary, this background pressure should also exist outside the configuration to maintain the force balance, particularly, preventing the configuration's disruption by the internal forces (the so-called hoop force).

[1] In *Jin et al.* [2017b] and papers cited therein R_s is denoted as r_1. Also, the magnetic field magnitude is expressed in terms of a parameter, a_1, the unit for this parameter being gauss/$R_\odot^2$ (note the typo in the note to Table 1 in *Jin et al.* [2017b]). The relationship between the parameters in the CGS unit system is as follows: $\frac{B_0}{\mathrm{Gs}}\approx 13.17\frac{a_1}{\mathrm{Gs}/R_\odot^2}\frac{r_0^2}{R_\odot^2}$, where $13.17\approx -\frac{4\pi}{(\alpha_0 r_0)^2\beta_0}$.

A *radial stretching* proposed by *Gibson and Low* [1998] extends the spheromak solution to include the effect of solar gravity and/or the flux rope acceleration. The magnetic field and pressure distribution of the new equilibrium configuration in the heliocentric coordinates, $\mathbf{R}$, are expressed via those of the spheromak evaluated at the point $\mathbf{R}'(\mathbf{R}) = \left(1 + \frac{a}{R}\right)\mathbf{R}$, where $R' = R + a$. An arbitrary constant a is the distance of stretching. To keep the stretched field divergence-free, one needs to additionally scale it. The final expression for the field is:

$$\mathbf{B}(\mathbf{R}) = \frac{R'}{R}\left(\mathbb{I} + \frac{a}{R}\mathbf{e}_R\mathbf{e}_R\right)\cdot\mathbf{B}_\mathrm{s}\left(\mathbf{R}' - \mathbf{R}_\mathrm{s}\right) \tag{4}$$

where $\mathbf{e}_R = \mathbf{R}/R$ and $\mathbb{I}$ is the identity matrix. The plasma pressure of the stretched magnetic configuration is defined as:

$$P(\mathbf{R}) = \left(\frac{R'}{R}\right)^2\left(P_\mathrm{s}\left(\mathbf{R}' - \mathbf{R}_\mathrm{s}\right) - \frac{a}{R}\left(2 + \frac{a}{R}\right)\frac{B^2_{\mathrm{s}R}\left(\mathbf{R}' - \mathbf{R}_\mathrm{s}\right)}{2\mu_0}\right) \tag{5}$$

Substituting expressions from Eqs. 4 and 5 into Eq. 1 results in the radial force, F_R, from the added tension of the stretched magnetic field, $\frac{1}{\mu_0}(\nabla\times\mathbf{B})\times\mathbf{B} - \nabla P = F_R\mathbf{e}_R$. This excessive force may balance the gravity acting on the density profile, if:

$$\rho = \frac{F_R}{g(R)} \tag{6}$$

where $\mathbf{g}(R) = -GM_\odot/R^2\mathbf{e}_R$, G is the gravitational constant, $M_\odot$ is the solar mass. Eq. 6 results, however, in negative density. In reality this corresponds to regions with depleted plasma density compared to the background. In fact, one can superimpose the configuration defined by Eqs. 4, 5 and 6 over any barometric atmosphere, $P_\mathrm{bar}(\mathbf{R})$ and $\rho_\mathrm{bar}(\mathbf{R})$, while retaining the equilibrium condition:

$$\frac{1}{\mu_0}(\nabla\times\mathbf{B})\times\mathbf{B} - \nabla\left(P + P_\mathrm{bar}\right) + \left(\rho + \rho_\mathrm{bar}\right)\mathbf{g} = 0 \tag{7}$$

As a result of the transformation, the spherical configuration is stretched towards the heliocenter as shown in the left panel in Fig. 1. If thus defined flux rope has an initial velocity profile $\mathbf{u} \propto \mathbf{R}$, or if the radial tension is applied to a reduced density in the configuration, $\rho = \frac{F_R}{g(R)+A(R)}$, to produce an acceleration in the radial direction, $\mathbf{A} \propto \mathbf{R}$, it would self-similarly travel away from the Sun [*Gibson and Low*, 1998], i.e. mimic behavior of a CME.

When the solution represented by Eq. 4, 5, 6 is superimposed onto the existing corona, the sharper end of the teardrop shape is submerged below the solar surface. In the wider top part of the configuration ("balloon") the density variation in Eq. 6 is *negative*, which makes the resulting density lower than that of the ambient barometric background. As the result, the Archimedes (buoyancy) force acting on this part pulls the whole configuration away from the Sun. Such structure is consistent with the commonly observed three-part CME configuration consisting of a bright leading loop enclosing a dark low-density cavity contain-

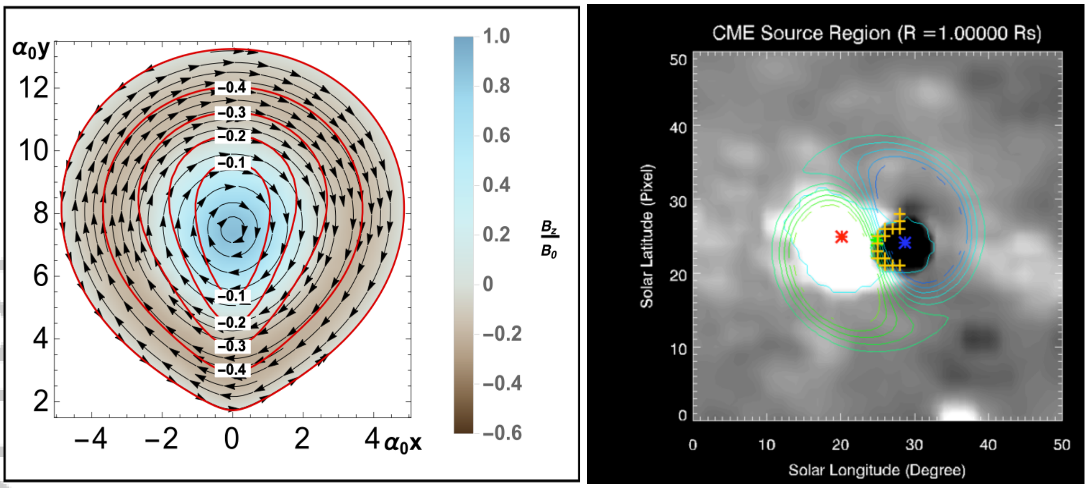

Figure 1. **Left**: Equatorial plane of the stretched flux rope for $\beta_0 = -2.87\times10^{-2}$. The original flux rope is placed by distance R_s=1.6r_0 along a direction in the equatorial plane and then stretched towards the heliocenter by distance a=0.3r_0. Magnetic field direction is marked with arrows, off-plane component of the magnetic field is normalized per B_0 and shown by color. Local values of plasma parameter $\beta(\mathbf{r}) = \mu_0 P(\mathbf{r})/B^2(\mathbf{r})$ are shown with red curves corresponding to levels $\beta = -0.1, -0.2, -0.3, -0.4$. **Right**: The zoomed-in AR as seen in the GONG magnetogram. By clicking on the white (positive) and black (negative) spots, EEGGL calculates the GL configuration parameters. The radial magnetic field levels of the recommended GL configuration is shown with the contour lines. The S-shaped polarity inversion line of the GL configuration, separating the cusped contours, overlaps with that of the AR (yellow crosses).

ing a high-density core [e.g. *Hundhausen*, 1993; *Howard et al.*, 1997]. The core of the structure, the narrower Sun-ward part of the configuration with excessive *positive* density, is typically considered to be filament material. The prominence material is often visible in the EUV at 304 Å) where it corresponds with the the CME core [e.g. *Davis et al.*, 2009; *Liu et al.*, 2010] The tip of the configuration with the magnetic field lines both ingoing and outgoing from the solar surface is anchored to the negative and positive magnetic spots of a bipolar active region (see the right panel in Fig. 1), considered as the source of the CME. Depending on the reconnection rate, the configuration, while it travels toward 1 AU, can either keep being magnetically connected to the AR, or it may disconnect and close.

Self-similarity of the propagation isn't strictly retained in the realistic corona: in order for the configuration to remain at force-equilibrium and therefore propagate in a self-similar fashion, a confining shape needs to have a specific distribution of the external pressure and velocity, which linearly increases with radial distance. The self-similarity breaks down, when solar wind approaches its terminal velocity, i.e. stops accelerating. Realistic distribution of pressure in the coronal plasma leads to the pressure imbalance, i.e.

the loss of equilibrium, one of the key assumptions of GL approach. Also, coronal magnetic field exerts Ampere's force onto the flux rope's current, thus further contributing to the force imbalance. This effect may be reduced by choosing a more realistic value of β_0, e.g. β_0=0, which would allow canceling the background magnetic field, at least partially, within the flux rope. Nevertheless, numerical studies [e.g. *Manchester et al.*, 2004b,a; *Lugaz et al.*, 2005; *Jin et al.*, 2017a] showed that the evolution of the flux rope is approximately self-similar to a distance of 40-50 $R_\odot$. which provides a certain predictability of the subsequent CME transport. This, ultimately, defines the suitability of GL flux rope as a tool for initiating CMEs with predefined properties and led to the development of EEGGL.

EEGGL [2] is a user-friendly tool developed by *Jin et al.* [2017b] and successfully transitioned to the Community Coordinated Modeling Center (CCMC). It integrates solar images of the eruption into an intuitive GUI that allows the user to set the parameters of the GL flux rope, which is designed to model a magnetically driven CME and its propagation to 1 AU. EEGGL incorporates magnetograms of the solar magnetic field prior to the eruption, and, if possible, the multi-point coronagraph observations of the CME near the Sun. As seen above, for a fixed $\beta_0 = -2.87\times10^{-2}$ a non-accelerating GL flux rope is fully defined by the set of free parameters $\mathbf{R}_s$, a, r_0, $\mathbf{B}_0$, σ_h. In the current implementation of EEGGL σ_h is chosen according to the hemispheric helicity rule (±1 for southern/northern hemisphere), while R_s=1.8$R_\odot$ and a=0.6$R_\odot$ are fixed. Also, the magnetic field vector, B_0, has no radial component. Thus, EEGGL needs to determine 5 remaining free parameters: latitude and longitude of the flux rope's center, orientation of the flux rope's axis, its size, r_0, and characteristic strength of the magnetic field, B_0. All parameters are computed based on the pre-eruptive magnetogram and user's input: the choice of an active region (AR), from which the CME originates, and its speed. The latter together with the magnetogram defines B_0 [see *Jin et al.*, 2017b]. The CME speed is obtained with the help of the STEREOCat [3] web-application available at the CCMC, which allows the user to derive both the CME speed and an approximate source location. For detailed instructions we refer readers to EEGGL web-site[2]. Using these inputs EEGGL automatically (1) processes the magnetogram; (2) analyzes and calculates the integral parameters of the AR; (3) automatically calculates the parameters of the GL flux rope; and finally (4) visualizes the magnetic field of the AR and of the GL configuration to verify that they match (see the right panel in Fig. 1).

EEGGL is not an independent tool and one requires a numerical heliospheric model to perform the actual simulation. The flux rope parameters produced by EEGGL can readily be used to initiate a CME sim-

[2] Available at `https://ccmc.gsfc.nasa.gov/eeggl/`

[3] Available at `https://ccmc.gsfc.nasa.gov/analysis/stereo/`

ulation in Space Weather Modeling Framework (SWMF) [*Tóth et al.*, 2012] either at the CCMC's computational facilities (the link is provided to users together with the results), or manually elsewhere. The parameters may also be used by any numerical heliospheric models, e.g. ENLIL [*Odstrčil*, 2003], SUSANOO-CME [*Shiota and Kataoka*, 2016] or EUHFORIA [*Poedts and Pomoell*, 2017], that supports CME initiation.

The primary source of criticism of EEGGL is the overall validity of representing CME by the flux rope of *Gibson and Low* [1998]. Although all published research to the date succeeds in doing so, the range of applicability of the approach isn't known. On the other hand, EEGGL presents a suitable tool for exploration and finding the conditions, when the technique fails to launch a successful CME.

The advantage of EEGGL as a community-wide available tool is simplicity of its interface. The AR is chosen by mouse-click on a magnetogram's image, the rest of the procedure is fully automated. This allows any user to set simulation parameters in a matter of minutes and focus on studying the physics of the process rather than the technical details of setting such simulation. At the moment, EEGGL is a unique tool that simplifies the interaction between a user and sophisticated numerical heliospheric models.

However, EEGGL hasn't reached its functionality limits and may be further improved. The further development will proceed along the following directions. The helicity of the flux rope, instead of being fixed for each hemisphere, will be derived from a vector magnetic field observations [e.g. Space-weather HMI Active Region Patches, SHARPs, *Bobra et al.*, 2014]. More control over the CME propagation will be achieved by applying special variations of the density profile of the flux rope, which results in an accelerated/decelerated self-similar motion [see *Gibson and Low*, 1998]. Incorporating such a feature would increase the functionality and range of the application of EEGGL and is the likely next step of its development. Additionally, EEGGL may be complemented with more precise methods of determining CME's speed in the early phase of eruption, e.g. via estimation of the reconnected flux using post-eruption arcades [*Gopalswamy et al.*, 2017], or through the relationship between the EUV dimming and resulting CME speed [*Mason et al.*, 2016]. Implementing new features requires adding new parameters to the model accompanied with extensive testing and validation via comparison with observational data.

The expected contribution of EEGGL to the community is yet to be measured, but one may expect a significant increase in the number of CME-related works and publications. This would provide opportunities for more detailed numerical studies of the process itself as well as related phenomena.

Acknowledgments: M. Jin's research is supported by NASA's SDO/AIA contract (NNG04EA00C) to LMSAL. The collaboration between the CCMC and University of Michigan is supported by the NSF SHINE grant 1257519 (PI Aleksandre Taktakishvili). The work performed at the University of Michigan was partially supported by National Science Foundation grants AGS-1322543 and PHY-1513379, NASA grant NNX13AG25G, the European Union's Horizon 2020 research and innovation program under grant agreement No 637302 PROGRESS. We would also like to acknowledge high-performance computing support from: (1) Yellowstone (ark:/85065/d7wd3xhc) provided by NCAR's Computational and Information Systems Laboratory, sponsored by the National Science Foundation, and (2) Pleiades operated by NASA's Advanced Supercomputing Division.

References

Bobra, M. G., X. Sun, J. T. Hoeksema, M. Turmon, Y. Liu, K. Hayashi, G. Barnes, and K. D. Leka (2014), The Helioseismic and Magnetic Imager (HMI) Vector Magnetic Field Pipeline: SHARPs - Space-Weather HMI Active Region Patches, *Sol. Phys.*, *289*, 3549–3578, doi:10.1007/s11207-014-0529-3.

Cliver, E. W. (2009), History of research on solar energetic particle (SEP) events: the evolving paradigm, in *Universal Heliophysical Processes*, *IAU Symposium*, vol. 257, edited by N. Gopalswamy and D. F. Webb, pp. 401–412, doi:10.1017/S1743921309029639.

Davis, C. J., J. A. Davies, M. Lockwood, A. P. Rouillard, C. J. Eyles, and R. A. Harrison (2009), Stereoscopic imaging of an Earth-impacting solar coronal mass ejection: A major milestone for the STEREO mission, *Geophys. Res. Lett.*, *36*, L08102, doi:10.1029/2009GL038021.

Dryer, M., Z. Smith, C. D. Fry, W. Sun, C. S. Deehr, and S.-I. Akasofu (2004), Real-time shock arrival predictions during the "Halloween 2003 epoch", *Space Weather*, *2*, S09001, doi:10.1029/2004SW000087.

Fry, C. D., W. Sun, C. S. Deehr, M. Dryer, Z. Smith, S.-I. Akasofu, M. Tokumaru, and M. Kojima (2001), Improvements to the HAF solar wind model for space weather predictions, *J. Geophys. Res.*, *106*, 20,985–21,002, doi:10.1029/2000JA000220.

Gibson, S. E., and B. C. Low (1998), A Time-Dependent Three-Dimensional Magnetohydrodynamic Model of the Coronal Mass Ejection, *Astrophys. J.*, *493*, 460–473, doi:10.1086/305107.

Gopalswamy, N. (2009), Coronal mass ejections and space weather, in *Climate and Weather of the Sun-Earth System (CAWSES): Selected Papers from the 2007 Kyoto Symposium*, edited by T. Tsuda, R. Fujii, K. Shibata, and M. A. Geller, pp. 77–120.

Gopalswamy, N., A. Lara, S. Yashiro, M. L. Kaiser, and R. A. Howard (2001), Predicting the 1-AU arrival times of coronal mass ejections, *J. Geophys. Res.*, *106*, 29,207–29,218, doi:10.1029/2001JA000177.

Gopalswamy, N., S. Yashiro, S. Akiyama, and H. Xie (2017), Estimation of Reconnection Flux Using Post-eruption Arcades and Its Relevance to Magnetic Clouds at 1 AU, *Sol. Phys.*, *292*, 65, doi:10.1007/s11207-017-1080-9.

Grad, H., and H. Rubin (1958), Hydromagnetic Equilibria and Force-Free Fields, in *Proceedings of the 2nd UN Conference on the Peaceful Uses of Atomic Energy*, vol. 31, pp. 190–197.

Hakamada, K., and S.-I. Akasofu (1982), Simulation of three-dimensional solar wind disturbances and resulting geomagnetic storms, *Space Sci. Rev.*, *31*, 3–70, doi:10.1007/BF00349000.

Hayashi, K., X. P. Zhao, and Y. Liu (2006), MHD simulation of two successive interplanetary disturbances driven by cone-model parameters in IPS-based solar wind, *Geophys. Res. Lett.*, *33*, L20103, doi:10.1029/2006GL027408.

Howard, R. A., G. E. Brueckner, O. C. St. Cyr, D. A. Biesecker, K. P. Dere, M. J. Koomen, C. M. Korendyke, P. L. Lamy, A. Llebaria, M. V. Bout, D. J. Michels, J. D. Moses, S. E. Paswaters, S. P. Plunkett, R. Schwenn, G. M. Simnett, D. G. Socker, S. J. Tappin, and D. Wang (1997), Observations of CMEs from SOHO/LASCO, *Washington DC American Geophysical Union Geophysical Monograph Series*, *99*, 17–26, doi:10.1029/GM099p0017.

Hundhausen, A. J. (1993), Sizes and Locations of Coronal Mass Ejections - SMM Observations from 1980 and 1984-1989, *J. Geophys. Res.*, *98*, 13,177, doi:10.1029/93JA00157.

Jin, M., C. J. Schrijver, M. C. M. Cheung, M. L. DeRosa, N. V. Nitta, and A. M. Title (2016), A Numerical Study of Long-range Magnetic Impacts during Coronal Mass Ejections, *Astrophys. J.*, *820*, 16, doi:10.3847/0004-637X/820/1/16.

Jin, M., W. B. Manchester, B. van der Holst, I. Sokolov, G. Tóth, A. Vourlidas, C. A. de Koning, and T. I. Gombosi (2017a), Chromosphere to 1 AU simulation of the 2011 March 7th event: A comprehensive study of coronal mass ejection propagation, *Astrophys. J.*, *834*(2), 172, doi:10.3847/1538-4357/834/2/172.

Jin, M., W. B. Manchester, B. van der Holst, I. Sokolov, G. Tóth, R. E. Mullinix, A. Taktakishvili, A. Chulaki, and T. I. Gombosi (2017b), Data-constrained coronal mass ejections in a global magnetohydrodynamics model, *Astrophys. J.*, *834*(2), 173, doi:10.3847/1538-4357/834/2/173.

Kataoka, R., T. Ebisuzaki, K. Kusano, D. Shiota, S. Inoue, T. T. Yamamoto, and M. Tokumaru (2009), Three-dimensional MHD modeling of the solar wind structures associated with 13 December 2006 coronal mass ejection, *Journal of Geophysical Research (Space Physics)*, *114*, A10102, doi:10.1029/2009JA014167.

Kay, C., N. Gopalswamy, A. Reinard, and M. Opher (2017), Predicting the Magnetic Field of Earth-impacting CMEs, *Astrophys. J.*, *835*, 117, doi:10.3847/1538-4357/835/2/117.

Lakhina, G. S., and B. T. Tsurutani (2016), Geomagnetic storms: historical perspective to modern view, *Geoscience Letters*, *3*, 5, doi:10.1186/s40562-016-0037-4.

Landau, L. D., and E. M. Lifshitz (1960), *Electrodynamics of continuous media*, Pergamon Press: Oxford.

Liu, Y., J. A. Davies, J. G. Luhmann, A. Vourlidas, S. D. Bale, and R. P. Lin (2010), Geometric Triangulation of Imaging Observations to Track Coronal Mass Ejections Continuously Out to 1 AU, *Astrophys. J. Lett.*, *710*, L82–L87, doi:10.1088/2041-8205/710/1/L82.

Lugaz, N., W. B. Manchester, IV, and T. I. Gombosi (2005), Numerical simulation of the interaction of two coronal mass ejections from sun to earth, *Astrophys. J.*, *634*, 651–662, doi:10.1086/491782.

Lugaz, N., W. B. Manchester, IV, I. I. Roussev, G. Tóth, and T. I. Gombosi (2007), Numerical Investigation of the Homologous Coronal Mass Ejection Events from Active Region 9236, *Astrophys. J.*, *659*, 788–800, doi:10.1086/512005.

Manchester, W. B., T. I. Gombosi, I. Roussev, A. Ridley, D. L. De Zeeuw, I. V. Sokolov, K. G. Powell, and G. Tóth (2004a), Modeling a space weather event from the Sun to the Earth: CME generation and interplanetary propagation, *J. Geophys. Res.*, *109(A18)*, 2,107–2,122, doi:10.1029/2003JA010150.

Manchester, W. B., T. I. Gombosi, I. Roussev, D. L. De Zeeuw, I. V. Sokolov, K. G. Powell, G. Tóth, and M. Opher (2004b), Three-dimensional MHD simulation of a flux rope driven CME, *J. Geophys. Res.*, *109(A18)*, 1,102–1,119, doi:10.1029/2002JA009672.

Manchester, W. B., A. J. Ridley, T. I. Gombosi, and D. L. DeZeeuw (2006), Modeling the Sun-to-Earth propagation of a very fast CME, *Advances in Space Research*, *38*, 253–262, doi:10.1016/j.asr.2005.09.044.

Manchester, W. B., J. U. Kozyra, S. T. Lepri, and B. Lavraud (2014a), Simulation of magnetic cloud erosion during propagation, *J. Geophys. Res.*, *119*, 5449–5464, doi:10.1002/2014JA019882.

Manchester, W. B., IV, B. van der Holst, and B. Lavraud (2014b), Flux rope evolution in interplanetary coronal mass ejections: the 13 May 2005 event, *Plasma Physics and Controlled Fusion*, *56*(6), 064006, doi:10.1088/0741-3335/56/6/064006.

Mason, J. P., T. N. Woods, D. F. Webb, B. J. Thompson, R. C. Colaninno, and A. Vourlidas (2016), Relationship of EUV Irradiance Coronal Dimming Slope and Depth to Coronal Mass Ejection Speed and Mass, *Astrophys. J.*, *830*, 20, doi:10.3847/0004-637X/830/1/20.

Odstrčil (2003), Modeling 3-D solar wind structure, *Adv. Space Sci.*, *32*(4), A02106, doi:10.1029/2004JA010745.

Poedts, S., and J. Pomoell (2017), EUHFORIA: a solar wind and CME evolution model, in *EGU General Assembly Conference Abstracts*, *EGU General Assembly Conference Abstracts*, vol. 19, p. 7396.

Riley, P., C. T. Russell, C. A. de Koning, D. A. Biesecker, J. Linker, M. J. Owens, N. Lugaz, P. Martens, R. Angryk, A. Reinard, R. K. Ulrich, T. S. Horbury, V. J. Pizzo, Y. Liu, and T. Hoeksema (2015), Predicting the Interplanetary Magnetic Field using Approaches Based on Data Mining and Physical Models, *AGU Fall Meeting Abstracts*.

Rollett, T., C. Möstl, A. Isavnin, J. A. Davies, M. Kubicka, U. V. Amerstorfer, and R. A. Harrison (2016), ElEvoHI: A Novel CME Prediction Tool for Heliospheric Imaging Combining an Elliptical Front with Drag-based Model Fitting, *Astrophys. J.*, *824*, 131, doi:10.3847/0004-637X/824/2/131.

Savani, N. P., A. Vourlidas, A. Szabo, M. L. Mays, I. G. Richardson, B. J. Thompson, A. Pulkkinen, R. Evans, and T. Nieves-Chinchilla (2015), Predicting the magnetic vectors within coronal mass ejections arriving at Earth: 1. Initial architecture, *Space Weather*, *13*, 374–385, doi:10.1002/2015SW001171.

Shafranov, V. D. (1966), Plasma Equilibrium in a Magnetic Field, *Rev. Plasma Phys.*, *2*, 103.

Shiota, D., and R. Kataoka (2016), Magnetohydrodynamic simulation of interplanetary propagation of multiple coronal mass ejections with internal magnetic flux rope (SUSANOO-CME), *Space Weather*, *14*(2), 56–75, doi:10.1002/2015SW001308.

Titov, V. S., and P. Démoulin (1999), Basic Topology of Twisted Magnetic Configurations in Solar Flares, *Astron. & Astrophys.*, *351*, 707–720.

Tóth, G., B. van der Holst, I. V. Sokolov, D. L. De Zeeuw, T. I. Gombosi, F. Fang, W. B. Manchester, X. Meng, D. Najib, K. G. Powell, Q. F. Stout, A. Glocer, Y.-J. Ma, and M. Opher (2012), Adaptive numerical algorithms in space weather modeling, *Journal of Computational Physics*, *231*, 870–903, doi:10.1016/j.jcp.2011.02.006.

Webb, D. F. (1995), Coronal mass ejections: The key to major interplanetary and geomagnetic disturbances, *Reviews of Geophysics Supplement*, *33*, 577–583, doi:10.1029/95RG00345.

Webb, D. F. (2000), Coronal mass ejections: origins, evolution, and role in space weather, *IEEE Transactions on Plasma Science*, *28*, 1795–1806, doi:10.1109/27.902209.

Zhao, X. P., S. P. Plunkett, and W. Liu (2002), Determination of geometrical and kinematical properties of halo coronal mass ejections using the cone model, *Journal of Geophysical Research (Space Physics)*, *107*, 1223, doi:10.1029/2001JA009143.

Figure1.1.

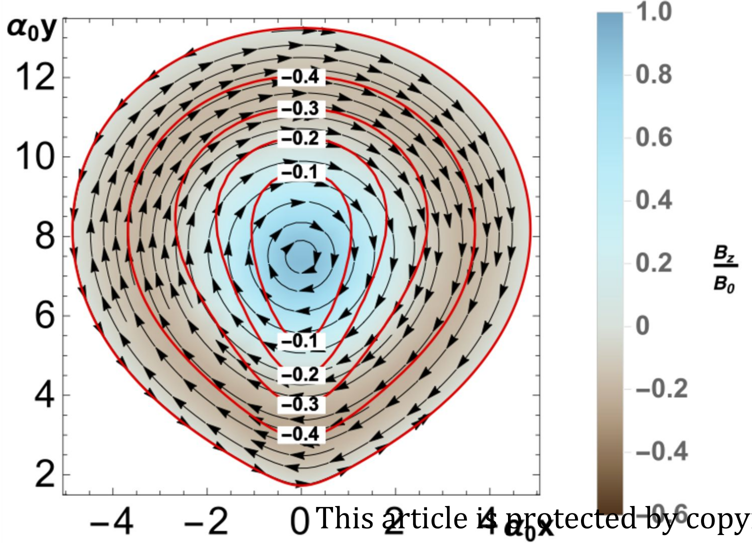
$\alpha_0 y$
12
10
8
6
4
2
−4
−2
0
2
4
$\alpha_0 x$
−0.4
−0.3
−0.2
−0.1
−0.1
−0.2
−0.3
−0.4
1.0
0.8
0.6
0.4
0.2
0
−0.2
−0.4
−0.6
$\frac{B_z}{B_0}$

Figure1.2.

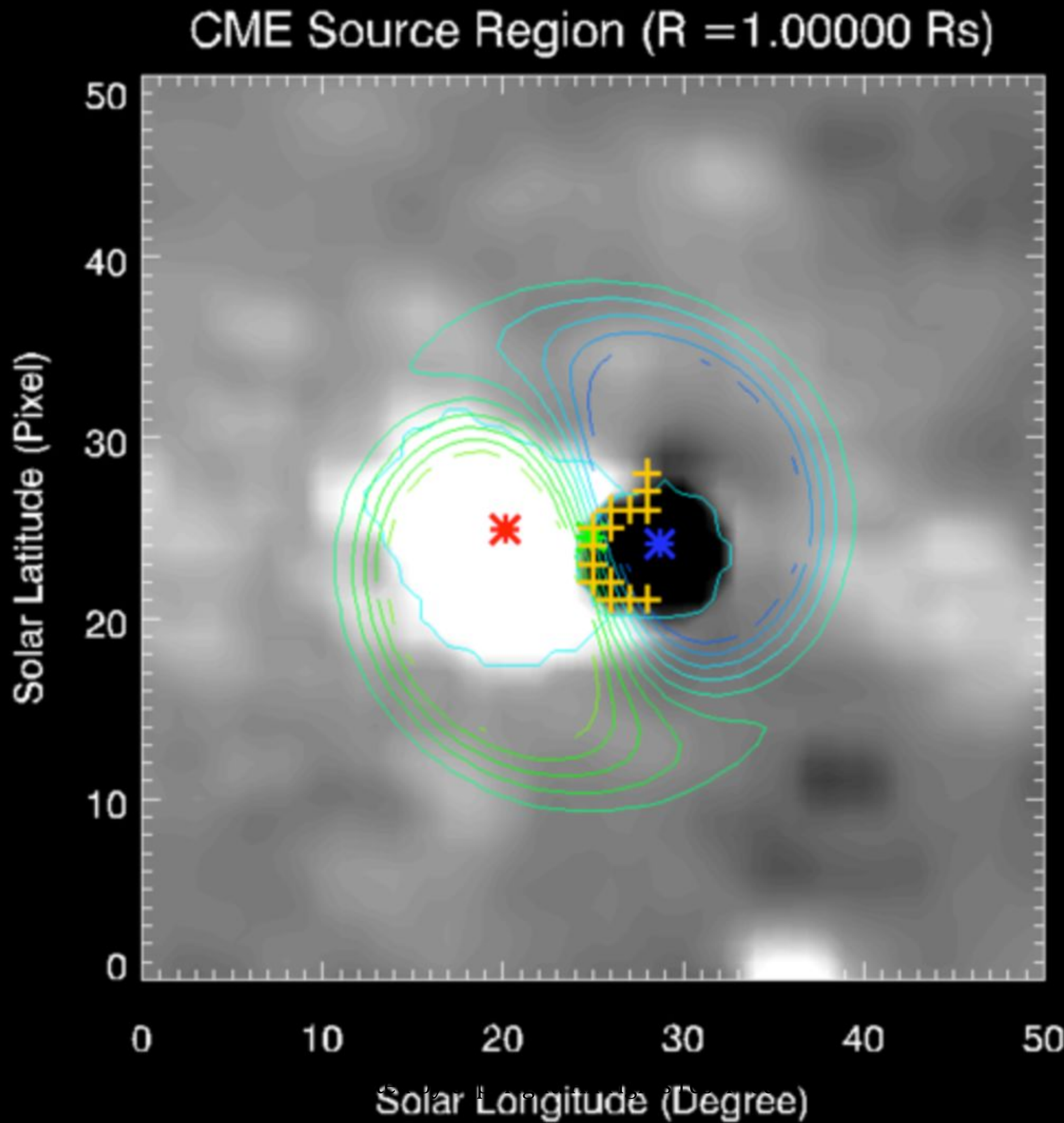
CME Source Region (R =1.00000 Rs)
Solar Latitude (Pixel)
Solar Longitude (Degree)
0
10
20
30
40
50

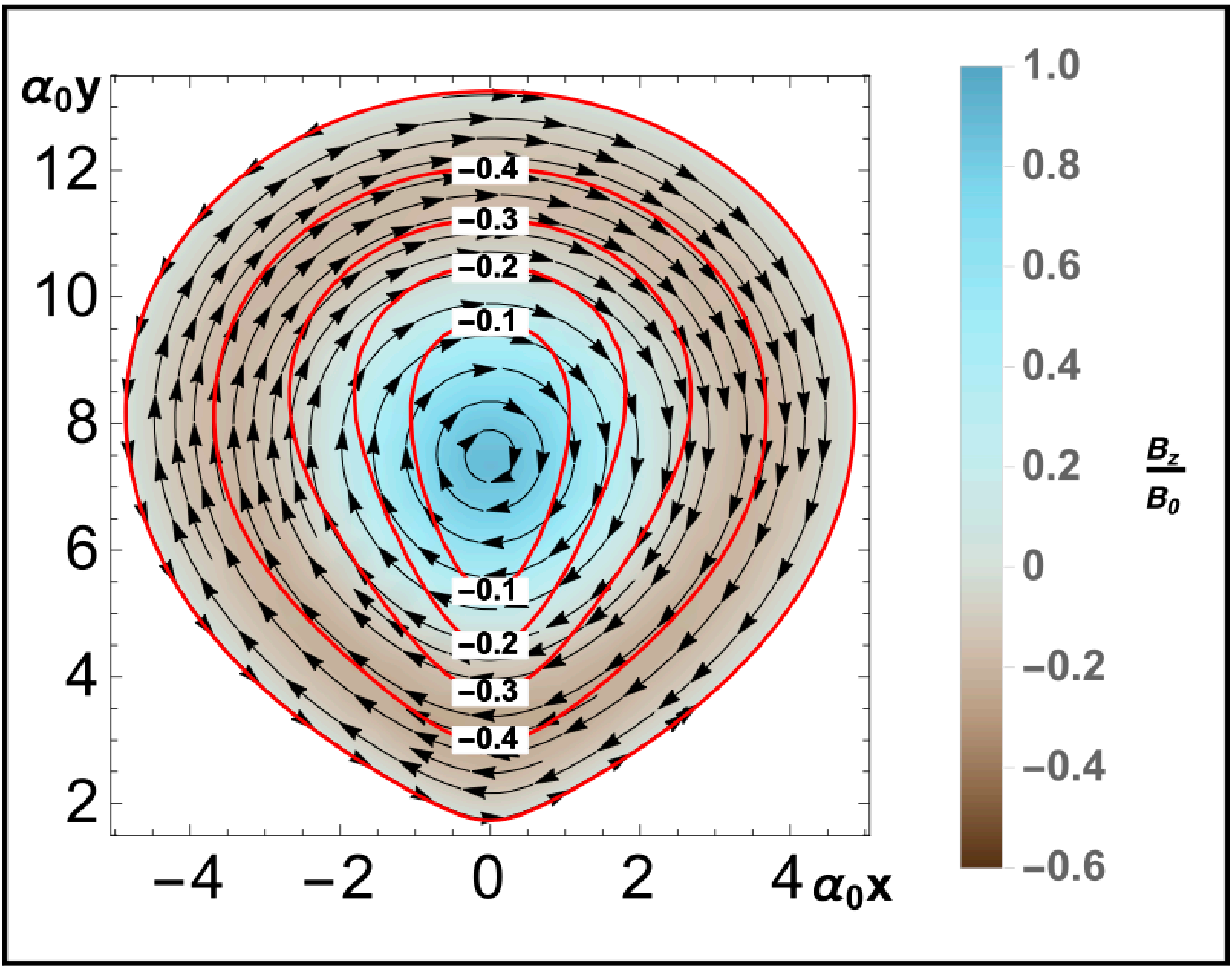

2017JA024304-f01-z-.png

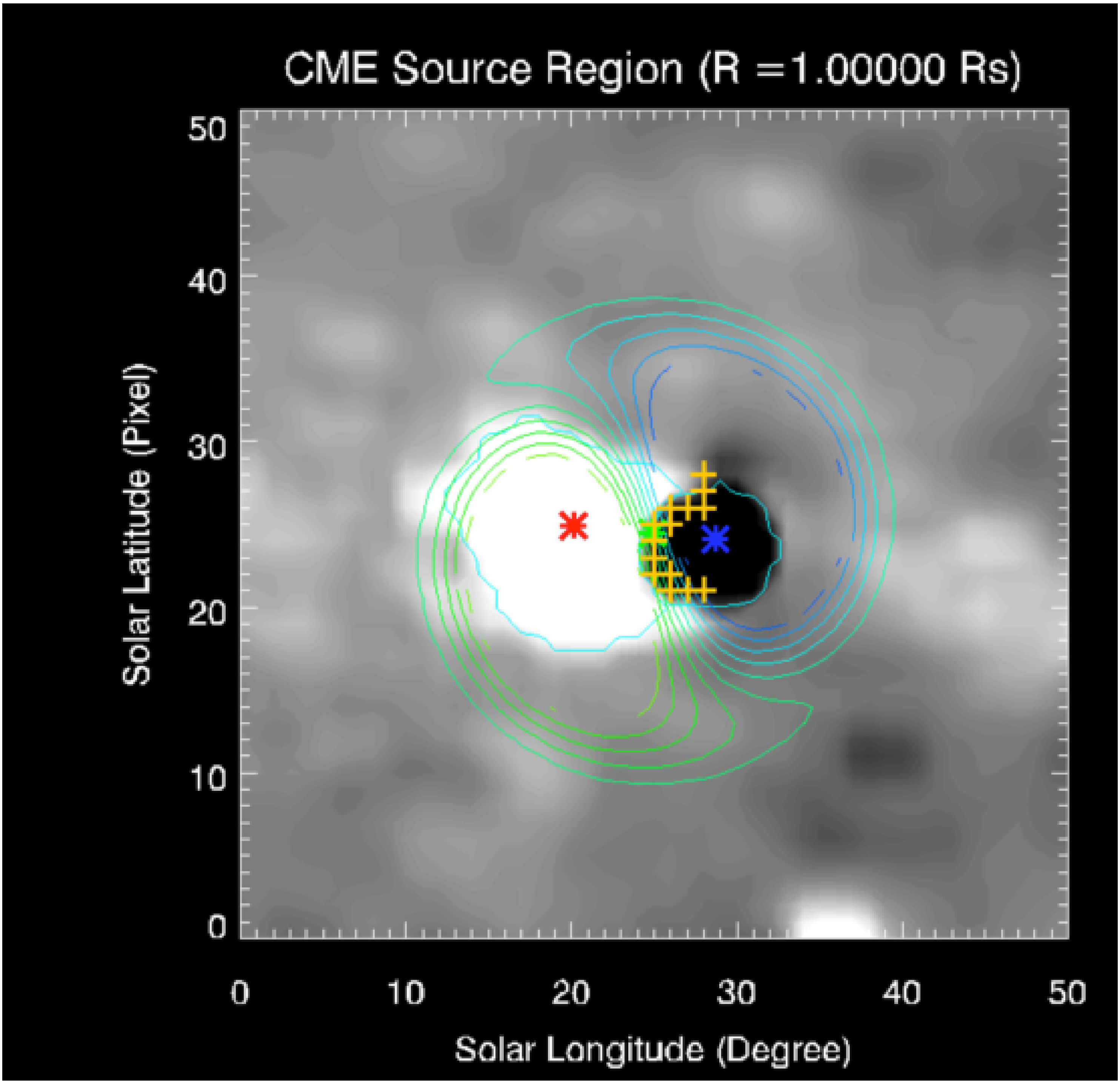

2017JA024304-f02-z-.png